batteries

MDPI

Article

Carbon-Coated Si Nanoparticles Anchored on Three-Dimensional Carbon Nanotube Matrix for High-Energy Stable Lithium-Ion Batteries

Hua Fang [1,2,3,*], Qingsong Liu [1], Xiaohua Feng [1], Ji Yan [1,2,3], Lixia Wang [1,2,3], Linghao He [1,*], Linsen Zhang [1,2,3,*] and Guoqing Wang [1,*]

[1] College of Material and Chemical Engineering, Zhengzhou University of Light Industry, Zhengzhou 450001, China
[2] Ceramic Materials Research Center, Zhengzhou University of Light Industry, Zhengzhou 450001, China
[3] Zhengzhou Key Laboratory of Green Batteries, Zhengzhou 450001, China
* Correspondence: fh@zzuli.edu.cn (H.F.); helinghao@zzuli.edu.cn (L.H.); hnlinsenzhang@163.com (L.Z.); gqwang@zzuli.edu.cn (G.W.)

Abstract: An easy and scalable synthetic route was proposed for synthesis of a high-energy stable anode material composed of carbon-coated Si nanoparticles (NPs, 80 nm) confined in a three-dimensional (3D) network-structured conductive carbon nanotube (CNT) matrix (Si/CNT@C). The Si/CNT@C composite was fabricated via in situ polymerization of resorcinol formaldehyde (RF) resin in the co-existence of Si NPs and CNTs, followed by carbonization at 700 °C. The RF resin-derived carbon shell (~10 nm) was wrapped on the Si NPs and CNTs surface, welding the Si NPs to the sidewall of the interconnected CNTs matrix to avoid Si NP agglomeration. The unique 3D architecture provides a highway for Li^+ ion diffusion and electron transportation to allow the fast lithiation/delithiation of the Si NPs; buffers the volume fluctuation of Si NPs; and stabilizes solid–electrolyte interphase film. As expected, the obtained Si/CNT@C hybrid exhibited excellent lithium storage performances. An initial discharge capacity of 1925 mAh g^{-1} was achieved at 0.1 A g^{-1} and retained as 1106 mAh g^{-1} after 200 cycles at 0.1 A g^{-1}. The reversible capacity was retained at 827 mAh g^{-1} when the current density was increased to 1 A g^{-1}. The Si/CNT@C possessed a high Si content of 62.8 wt%, facilitating its commercial application. Accordingly, this work provides a promising exploration of Si-based anode materials for high-energy stable lithium-ion batteries.

Keywords: lithium-ion batteries; silicon/carbon anode; carbon nanotubes; in situ polymerization; carbon coating

Citation: Fang, H.; Liu, Q.; Feng, X.; Yan, J.; Wang, L.; He, L.; Zhang, L.; Wang, G. Carbon-Coated Si Nanoparticles Anchored on Three-Dimensional Carbon Nanotube Matrix for High-Energy Stable Lithium-Ion Batteries. *Batteries* **2023**, *9*, 118. https://doi.org/10.3390/batteries9020118

Academic Editors: Atsushi Nagai and Carlos Ziebert

Received: 21 December 2022
Revised: 24 January 2023
Accepted: 30 January 2023
Published: 7 February 2023

1. Introduction

Lithium-ion batteries (LIBs) are widely applied to power sources for portable electronic equipment, power tools, electric vehicles, and even grid-scale energy storage systems [1–3]. Advanced LIBs with high energy density, high power density, and long cycle life are urgently needed to cater to the escalating energy density/power demands of the ever-developing portable electronic equipment and electric vehicles [4,5]. As the most successful anode material for current commercial LIBs, graphite materials are approaching their capacity limits and show limited application prospects in next-generation LIBs due to their relatively low theoretical capacity of ~372 mAh g^{-1} [6,7]. To significantly improve the energy density and power density, extensive research has focused on developing next-generation anode materials, including alloy-based anode materials (Si-based [8,9], Sn-based [10,11], Ge-based [12], etc.), transition metal compounds (oxides [13], sulfide [14], etc.) and metal–organic frameworks (MOFs) and their derivatives [15]. Among

all the candidates, silicon (Si) is considered a promising alternative for the currently employed graphite, as Si possesses the highest theoretical capacity (4200 mAh g^{-1} for $Li_{22}Si_5$ at 415 °C; 3579 mAh g^{-1} for $Li_{15}Si_4$ at room temperature) and relatively low lithium storage potential range (<0.4 V vs. Li/Li^+) [5,16,17].

However, extreme volume expansion/contraction (~300%) in the lithiation/delithiation process can cause Si particle pulverization, electrical contact deterioration, and solid–electrolyte interphase (SEI) instability, which further causes fast capacity decay and low Coulombic efficiency [8,18,19]. In addition, Si shows poor intrinsic electron conductivity, resulting in sluggish electrochemical kinetics and severely limiting the cycle life of the Si-based batteries [9,20]. To date, various strategies have been explored to develop the superior Si-based electrode materials, including the construction of Si nanostructures [21,22], porous Si [23–25], surface coating of protective layers [26–28], Si-based composites [17,29–31], SiO_x-based materials [32–34], and new electrode binders [35–39]. Of these, nano-Si materials have been shown to effectively relax the mechanical stress and strain on the electrode during volume fluctuation, avoiding cracking or pulverization of their structures, thereby significantly improving Coulombic efficiency and cyclability [30,40]. In this esteem, Si thin-film [2], Si nanowire [41], Si nanotube [21], and Si with nanoporous structure [42] have been extensively studied to improve the electrochemical performance of Si anodes. However, several challenges remain to be overcome in Si-based materials as anode material of LIBs. Firstly, nano-Si materials show a high specific surface area, leading to excessive formation of unstable SEI film and severe electrolyte decomposition [43]. Secondly, the repeated cracking/regeneration of the SEI films remains difficult to address [44]. Thirdly, Si nanoparticles (NPs) prefer to agglomerate due to their high surface energy, which makes it difficult to disperse Si NPs uniformly in the LIB electrode [45]. These challenges restrict the practical application of nano-Si anode materials.

To tackle the aforementioned problems, one of the most favorable strategies is to construct unique microstructures of Si/carbon (Si/C) composites, due to which carbon materials have the advantages of conductivity, structural stability, low cost, and ease of preparation [6,9]. The introduction of carbon can effectively enhance the rate capability and cycling performance of the Si anode. In this regard, various carbon materials such as porous carbon [46,47], carbon nanotubes (CNTs) [48,49], graphite [50,51], and graphene [52–54], have been composited with nano-Si to improve the cycling stability and rate capability of LIBs. The cross-linked CNT framework with high conductivity and mechanical flexibility can provide an electrically conductive pathway and accommodate the expansion of Si NPs [55]. Additionally, carbon coating, which aims to encapsulate Si NPs with carbon layers on their surface, can facilitate both the formation of stable SEI film and the enhancement of electronic conductivity [56]. Thus, ternary Si-based composites, which integrate Si NPs, carbon coating, and CNTs, have been constructed to produce voids between carbon shells, thereby buffering the volume change and enhancing high electrical conductivity. For example, An et al. [57] reported a three-dimensional (3D) hierarchical nano Si@C/CNT composite prepared via a self-electrostatic route, which exhibited high reversible capacity and outstanding rate performance when it was used as an anode material for LIBs. After enduring 1000 cycles at 0.5 C, it retained a high capacity of 989.5 mAh g^{-1} with high capacity retention of 86.6%. Zhang et al. [55] synthesized a Si/CNTs@(S)-C composite using spray-drying methods. The Si/CNTs@(S)-C composite delivered a high capacity of 943 mAh g^{-1} at a 0.2 C rate after 1000 cycles. Unfortunately, the recent reports on a Si-based anode usually contained a relatively low Si mass content to ensure their cycle stability, which weakens the high capacity superiority in commercial LIBs. Fabricating ternary Si/C/CNT composites with high Si content for next-generation LIBs via a low-cost and scalable route remains a significant challenge.

In this study, a 3D network structured Si/CNT@C composite anode material composed of Si NPs anchored on a conductive CNT matrix assisted by carbon coating, was designed and fabricated via a low-cost and scalable route for high-energy stable lithium-ion batteries. In situ resorcinol formaldehyde (RF) resin polymerization was carried out

in the co-existence of Si NPs and CNTs. Through carbonization at 700 °C under N_2 atmosphere, the resulting Si/CNT@RF resin composite was transformed into Si/CNT@C composite. The RF resin-derived carbon can act as an adhesive medium to weld Si NPs on the sidewall of CNTs, resulting in a stable 3D porous structure. Thus, the Si/CNT@C composite showed the advantages of buffering the volume fluctuation, restraining the agglomeration, facilitating fast ion/electron transportation, and stabilizing the SEI film. This unique material design enables the Si/CNT@C composite to deliver a high reversible 1106 mAh g^{-1} after 200 cycles at 0.1 A g^{-1}. The present work provides a facile and scalable strategy to construct the Si-based materials with high lithium storage capacity and excellent cycle stability.

2. Experimental Section

2.1. Chemicals and Reagents

All the chemicals were analytically pure and were used as received. Si powder with a particle size of 50~100 nm was purchased from Shanghai Pantian Powder Material Co., Ltd. (Shanghai, China). CNTs with an outer diameter of ~50 nm were purchased from Chengdu Organic Chemistry Co., Ltd. (Chengdu, China).

2.2. Material Preparation

2.2.1. Pretreatment of Si NPs and CNTs

The Si NPs were first pretreated in a mixed solution of ammonia (25 wt%), hydrogen peroxide (30 wt%), and deionized water with a volume ratio of 1:1:5 at 80 °C for 1 h under magnetic stirring. The pretreated Si NPs were collected via filtration, washed with distilled water, and dried in an oven at 60 °C for 12 h.

The CNTs were pretreated via refluxing in concentrated nitric acid for 6 h. After reflux, the oxidized CNTs were obtained via filtration, washed with deionized water, and finally dried in an oven at 60 °C for 12 h.

2.2.2. Preparation of Si/CNT@RF Resin Composites

For typical preparation, 0.3 g of pretreated Si NPs and 0.92 g of CTAB were ultrasonically dispersed into 28 mL deionized water for 30 min to form a homogeneous suspension. Then, ethanol (11 mL), resorcinol (0.28 g), ammonia (0.1 mL, 25 wt%), and pretreated CNTs (33.3 mg) were added and sonicated at room temperature for 30 min. Thirdly, 0.4 mL formaldehyde (37~40 wt%) was added to the homogeneous suspension. The in situ polymerization of RF resin was achieved through continuous stirring at 35 °C for 6 h and aging at room temperature for 12 h. Finally, the Si/CNT@RF resin composite was obtained via filtration, washed with deionized water and ethanol, and dried in an oven at 60 °C overnight.

2.2.3. Preparation of Si/CNT@C Composites

As for the preparation of the Si/CNT@C composite, the as-prepared Si/CNT@RF resin composite was heated under a N2 atmosphere at 700 °C for 3 h with a heating rate of 2 °C/min. Afterward, the tubular furnace was cooled naturally to room temperature. For comparison, the Si@C composite was also prepared with the same preparation process as the Si/CNT@C composite, but without adding CNTs in the in situ polymerization process.

2.3. Material Characterization

The crystal structures were determined via X-ray diffraction (XRD, Bruker D8 Advance, using Cu Kα) at a scan rate of 5° min^{-1}. The morphologies were characterized by field-emission scanning electron microscopy (FE-SEM, JEOL JSM-7001F). Transmission electron microscopy (TEM, JEOL JEM-2100) was employed to characterize the microstructures. The weight contents of Si NPs in composites were determined by thermogravimetric analysis under an air atmosphere (TGA, STA 449) with a heating rate of 10 °C min^{-1}.

Raman spectra were performed on a Raman spectrometer system (HORIBA Scientific LabRAM HR Evolution) with an excitation wavelength of 532 nm. X-ray photoelectron spectroscopy (XPS) of the powders was performed using an ESCALAB-250Xi with Al Kα radiation.

2.4. Electrochemical Characterization

The Si electrode, Si@C electrode and Si/CNT@C electrode were prepared via the same process with the bare Si power, Si@C, and Si/CNT@C as active materials, respectively. The electrode slurry was made by mixing the active material, conductive agent (Super P), and binder in a mass ratio of 8:1:1 with deionized water as a solvent. The binder was composed of styrene-butadiene rubber (SBR) and carboxymethyl cellulose (CMC) with a mass ratio of 3:2. The electrode slurry was pasted on copper foil using an automatic coating machine and vacuum dried at 120 °C for 8 h. The coating thickness of the slurry was set as 100 μm for the Si, Si@C and Si/CNT@C electrodes, resulting in comparable mass loading and thickness for all three kinds of electrodes. The obtained electrode film was punched into disc electrodes with a diameter of 14 mm and pressed under 15 MPa. Based on the mass loading of the Si/CNT@C electrode (~0.65 mg cm^{-1}), the mass content of active material (80%), and the bare Si mass ratio in the Si/CNT@C composite (62.8%), the mass loading of bare Si NPs for the Si/CNT@C electrode can be calculated as ~0.65 × 80% × 62.8% = ~0.33 mg cm^{-1}.

Electrochemical measurements were conducted at room temperature on CR2016 coin-type cells, which were fabricated in an argon-filled glove box (MB-10-G, MBRAUN). Lithium metal was used as the counter/reference electrode, Celgard 2400 membrane as the separator, and 1 M $LiPF_6$ in a 1:1:1 (volume ratio) mixture of ethylene carbonate (EC), dimethyl carbonate (DMC), and ethyl methyl carbonate (EMC) as the electrolyte solution. Cyclic voltammetry (CV) tests were carried out on a CHI 660E electrochemical workstation at a scanning rate of 0.1 mV s^{-1} between 1.5 and 0.01 V (vs. Li^+/Li). Galvanostatic charge/discharge (GCD) tests were performed at a cell voltage of 1.5–0.01 V (vs. Li^+/Li) on a Neware CT-4008T battery tester at different current rates. The GCD test currents was calculated based on the total mass active material. The specific capacity was obtained from $C_m = It/m$, where I represents the charge/discharge current (A); t is the charge/discharge time (s), and m is the total mass of the active material (g). As for the si/CNT@C electrode, the total mass of active material includes the carbon coating shell, CNT matrix, and Si NPs of the composite. Electrochemical impedance spectroscopy (EIS) tests were performed on a CHI 660E electrochemical workstation using newly installed coin-type cells (discharged state). The frequency range and voltage amplitude were 10^5~0.01 Hz and 5 mV, respectively.

3. Results and Discussions

3.1. Morphology, Microstructure and Crystalline Phase Studies

As illustrated in Figure 1a, the Si/CNT@RF resin composite was prepared through in situ polymerization of RF resin in the co-existence of the pretreated Si NPs and CNTs. The hydrophilic treated Si NPs exhibited plenty of Si-O-H surface functional groups after being dissolved in the water–ethanol–ammonia solution [58], while the acid-treated CNTs also possessed rich surface oxygen functional groups [59]. There is a strong hydrogen bonding force between the surface oxygen functional groups, facilitating the fine interface contact among Si NPs, CNTs, and RF resin (shown in Figure 1a). As a result, the RF resin grows directly on the surface of Si NPs and CNT in the in situ polymerization process, thereby forming a uniform RF resin coating shell on the surface of Si NPs and CNTs. During the in situ polymerization procedure, CTAB was used as a surfactant, which can improve the dispersion of Si NPs in the reaction solution and act as the soft template for the formation of a mesostructured RF resin coating shell [60]. After carbonization, the brown Si/CNT@RF resin composite was converted to black Si/CNT@C (Figure S1).

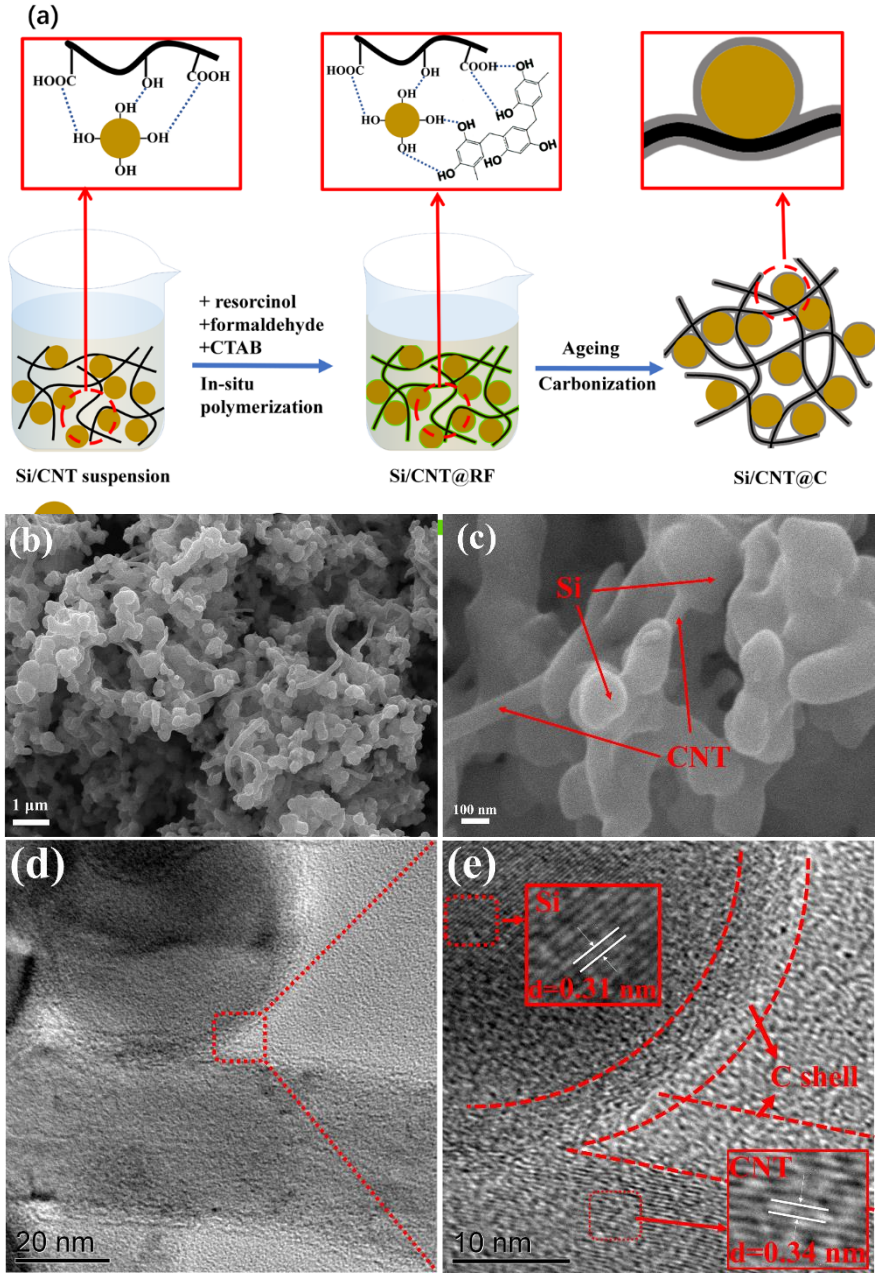

Figure 1. (**a**) Schematic illustration of the fabrication process, (**b**,**c**) SEM images, (**d**) TEM image, and (**e**) HR-TEM image of Si/CNT/C composite.

Figure 1b,c show the FE-SEM of Si/CNT@C composite, which exhibits a 3D nanoporous morphology. It can be clearly observed that Si NPs were well dispersed in the 3D interconnected CNT matrix without aggregation. The microstructure of Si/CNT@C composites was further characterized by TEM and HR-TEM images. As shown in Figure 1d, the RF resin-derived carbon shell, about ~10 nm thick, was uniformly coated on the surface of Si NPs and CNTs. The clear lattice fringe with spacing of 0.31 and 0.34 nm indexed to the (111) plane of the Si NPs and (002) plane of the CNT matrix appears in the high-resolution TEM (HR-TEM) image (Figure 1e) [61]. Here, the carbon coating shell used an adhesive medium, which attached Si NPs to the CNT sidewall and inhibited the aggregation of the Si NPs. Meanwhile, CNTs acted as "bridges" to string the isolated Si NPs together and provide a fast electron transport highway. Different from the Si NPs in the Si/CNT@C composite anchored on the CNT sidewall without agglomeration, the Si NPs

both in the bare Si sample and Si@C composite showed a certain level aggregate phenomenon due to their high surface energy (Figure S2). This result reveals that the presence of CNTs in the Si/CNT@C composite effectively avoids the agglomeration of Si NPs.

The XRD patterns of all the samples exhibit six diffraction peaks at 28.4°, 47.2°, 56.2°, 69.2°, 75.5°, and 88.1°, corresponding to (111), (220), (311), (400), (331), and (442) plane of the Si crystal (JCPDS no. 27-1402) [56,62]. In addition, a wide and weak peak centered at 24.5° can be observed in the Si@C and Si/CNT@C samples, which can be indexed to the (002) plane of the amorphous carbon coating layer and CNT matrix. Compared with the pattern of Si@C, the (002) peak of Si/CNT@C is much clearer due to the existence of CNTs. The existence of amorphous carbon and CNTs can be further confirmed by the Raman spectrum. As shown in Figure 2b, peaks at the wavenumbers of 136, 289, 509, and 924 cm^{-1} can be attributed to elemental Si [1,57,63]. The peaks at 1350 and 1590 cm^{-1} are indexed to the characteristic D and G peaks of carbon material, respectively. The D band is associated with the disordered carbon structure (sp^3-hybridized carbon), while the G band is attributed to an ordered graphitic lattice (E_{2g} phonon of sp^2-hybridized carbon) [62,64]. The relative intensity (I_D/I_G) of the D and G band is commonly used to detect the graphitization degree of carbon materials. The increase in I_D/I_G means the materials are more amorphous [65]. The I_D/I_G of the Si@C sample is 0.98, much larger than that of the Si/CNT@C sample (0.91), revealing that the RF resin-derived carbon coating is amorphous. This is consistent with the XRD results mentioned above.

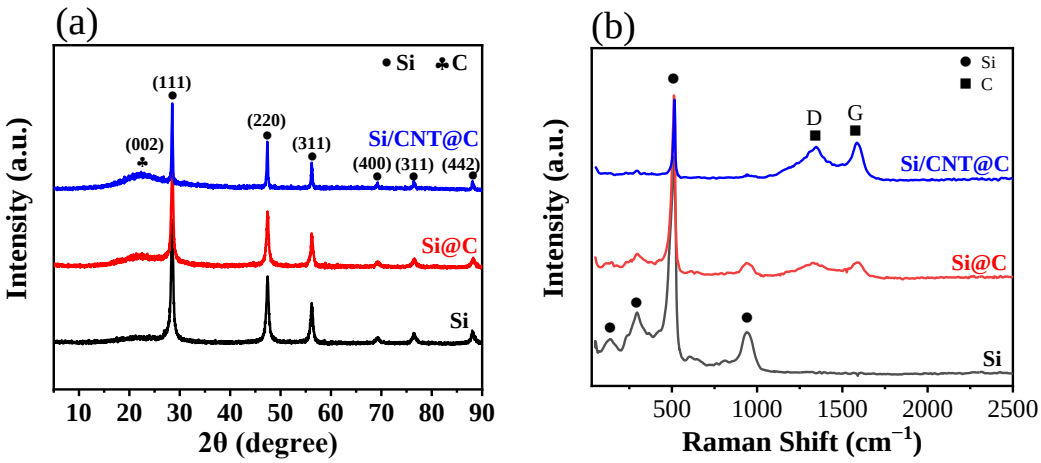

Figure 2. (**a**) XRD patterns and (**b**) Raman spectra of the samples.

The chemical state and molecular environment of the Si/CNT@C sample are further characterized by XPS spectra. As shown in Figure 3a, the signals of Si 2p (102.9 eV), C 1s (285.5), and O 1s (533.0) can be observed in XPS survey spectrum of the Si/CNT@C. The high-resolution XPS spectra of Si, C, and O elements contained in the Si/CNT@C composite were deconvoluted using software named XPSPEAK41, a baseline type of Shirley, and a Lorentzian–Gaussian distribution. The Si 2p XPS spectrum (Figure 3b) can be divided into five peaks, which are attributed to the Si–Si (99.1 and 99.8 eV) and Si–O (100.9, 103.1 and 103.9 eV) bonds, respectively [66]. The Si–O peak originated from the SiO_2 and SiO layer on the surface of Si NPs [67]. The surface of Si NPs is usually oxidized to form SiO_x, including SiO and SiO_2. The existence of SiO_x in the Si-based anode materials has been reported by some recent studies [1,43,66]. The C 1s spectrum in Figure 3c can be fitted to three peaks at 284.8, 286.5, and 289.0 eV, which are assigned to the C–C, C–O, and O–C=O bonds [66,68]. The O1s peak can be deconvoluted into Si–O (532.4 eV) and O–C=O (533.6 eV) bonds [69]. To acquire high specific capacity, it is vital to raise the Si mass content in the composite electrodes [1]. The mass contents of Si NPs were estimated according to the TG plots of Si, Si@C, and Si/CNT@C samples (Figure S3). As exhibited in Table S2, the Si/CNT@C composite contains a very high Si content of 62.8 wt%, which greatly exceeds

that of most recently reported Si-based anode materials, such as SMPS−1 (12.37 wt%) [70], GSCC (39.75 wt%) [66], Si/CNTs/C (40.4 wt%) [71], C/Si/CNT (42.17 wt%) [72], and Si@C@v@CNTs (14.1 wt%) [73]. Due to the high Si content of the as-prepared Si/CNT@C composite, high energy density can be expected to facilitate its commercial application.

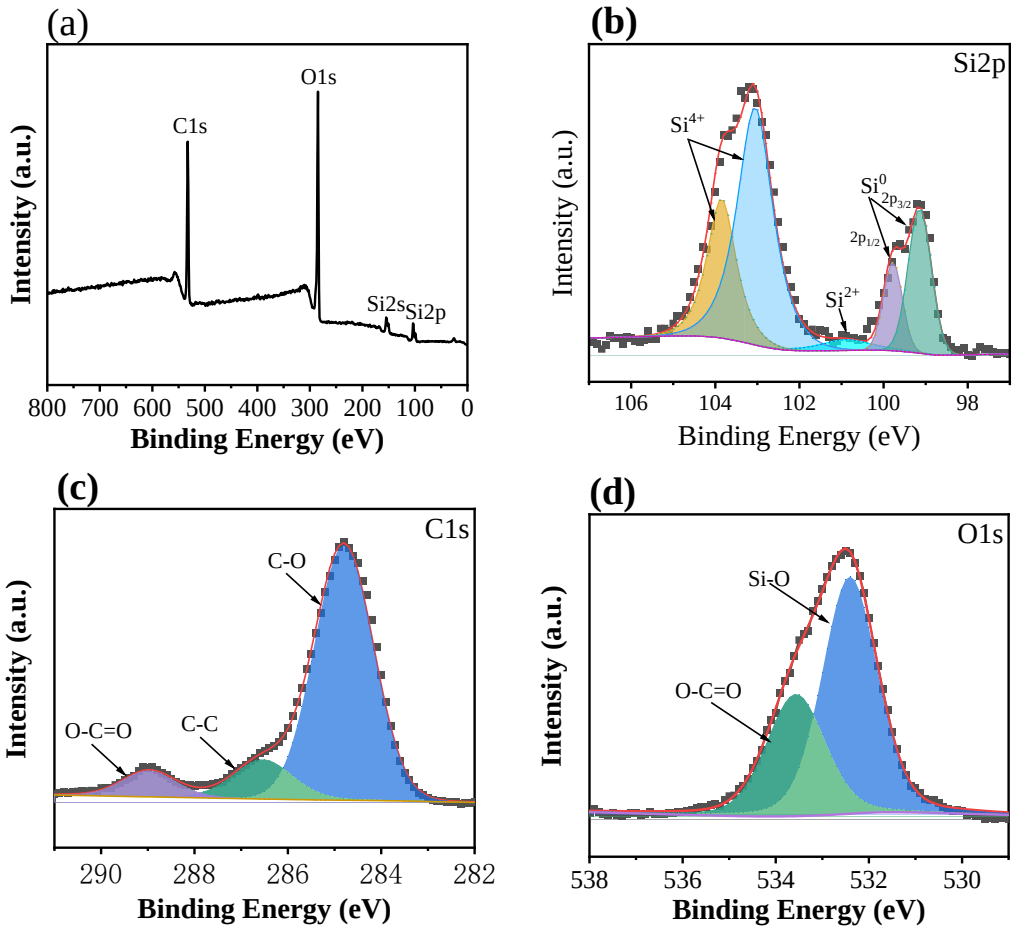

Figure 3. (**a**) XPS spectra, (**b**) Si2p, (**c**) C1s, and (**d**) O1s of Si/CNT@C sample.

3.2. Electrochemical Studies

To characterize the electrochemical behaviors of the Si/CNT@C composite, CV tests were first performed at a scan rate of 0.1 mV s^{-1} with a potential range of 0.01~1.5 V vs. Li/Li^+. As shown in Figure 4a, a weak and broad peak centered at 0.8 V in the first cathodic scan is ascribed to the decomposition of electrolyte and the formation of SEI film [43,55]. Such an irreversible peak did not show up in the subsequent cathodic scans, indicating that stable SEI film was achieved in the first cathodic CV scan [74]. The sharp peak below 0.1 V in the first cathodic scan corresponded to the lithiation of silicon to Li_xSi [75]. In the first anodic scan, the oxidation peaks at 0.32 and 0.47 V are recognized as the delithiation process of the Li_xSi phase to amorphous Si. The following CV scans show two reduction peaks at 0.22 and below 0.1 V, and two oxidation peaks at 0.32 and 0.47 V, corresponding to the reversible lithiation/delithiation behavior of amorphous silicon [76]. As the number of cycles increases, the peak intensity of the CV curves gradually increases, revealing an activation process [69,77]. The bare Si and Si@C electrodes show similar CV behaviors (Figure S4a,b). In contrast, the Si/CNT@C electrode showed the largest response current among the three kinds of electrodes, demonstrating the best lithium storage performance (Figure S4c).

The first three GCD curves of the Si/CNT@C, Si and Si@C electrodes at 0.1 A g^{-1} are exhibited in Figure 4b, Figure S5a and Figure S5b, respectively. In the charge curves of the

first GCD cycles, all the electrodes show slope charge plateaus between 1.5 V and 0.2 V and voltage plateaus at 0.1 V, which correspond to the irreversible SEI formation and lithiation of silicon to LixSi [43]. The slope charge plateau between 1.5 V and 0.2 V disappears in the charge curves of the following GCD cycles, indicating that SEI formation is completed in the first cycle. As for the discharge curves, the discharging plateaus are observed at 0.1 V, which corresponds to the delithiation process of the LixSi alloy. These results are consistent with the CV scanning of the Si/CNT@C electrode (Figure 4a). The initial discharge capacities were 1322, 1802, and 1925 mAh g^{-1}, and the initial Coulomb efficiencies were 61 %, 72%, and 78% for the Si, Si@C, and Si/CNT@C electrodes, respectively. The low initial Coulomb efficiencies are caused by irreversible formation of the SEI layer [78]. The Si/CNT@C electrode showed the largest discharge capacity and the highest Coulomb efficiency, which may be attributed to the synergistic effects of the carbon coating and CNT matrix.

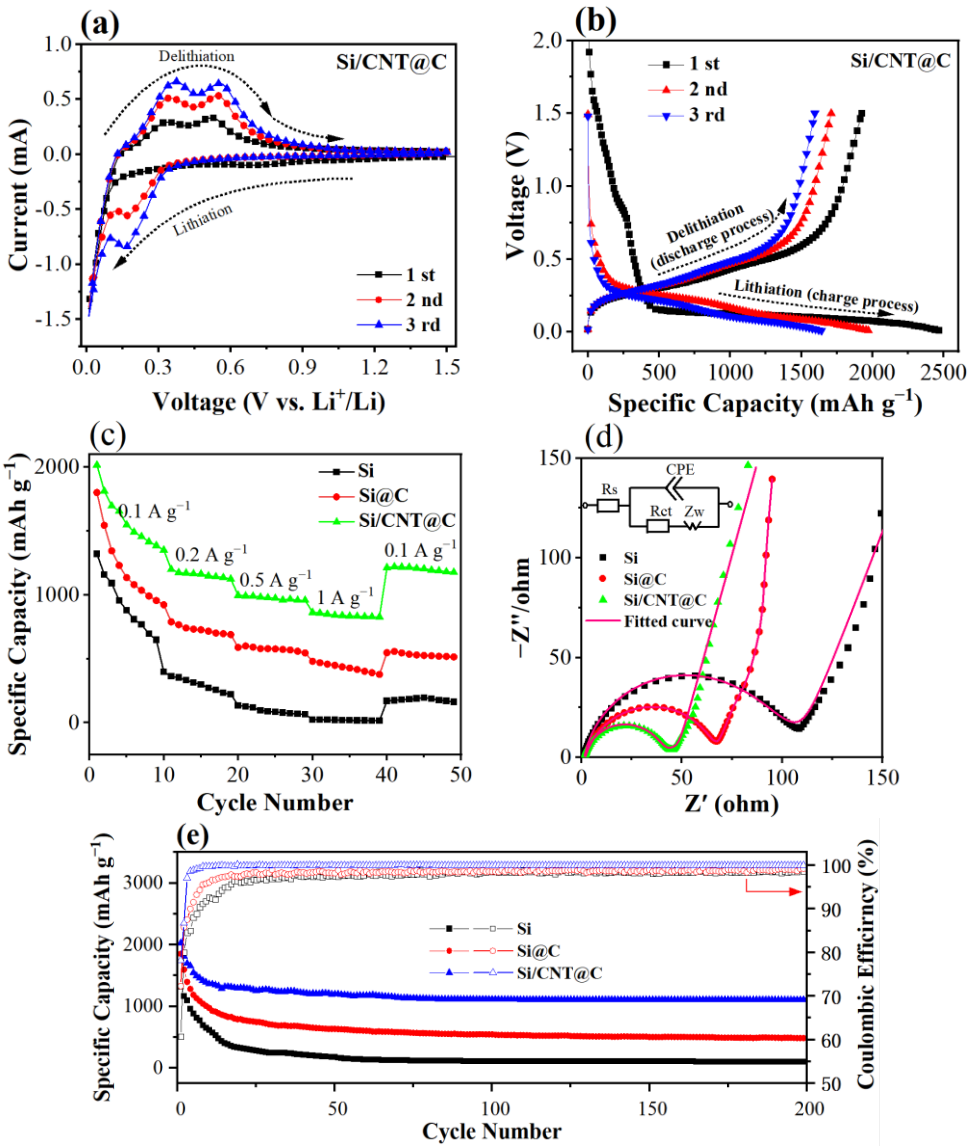

Figure 4. (**a**) CV curves of Si/CNT/C electrode at a scan rate of 0.1 mV s^{-1}. (**b**) Charge/discharge curves of Si/CNT/C electrode. (**c**) Rate performances of the bare Si, Si/C, and Si/CNT/C electrodes. (**d**) EIS curves (inset shows equivalent circuit) of the bare Si, Si/C, and Si/CNT/C electrodes. (**e**) Cycle performances of the bare Si, Si/C and Si/CNT/C electrodes.

Furthermore, the rate performances were investigated by GCD tests at different current densities. As shown in Figure 4c, the Si/CNT@C exhibits the best rate capability at all

current rates compared with those of the Si and Si@C. The Si/CNT@C showed a high charge capacity of 1387 mAh g^{-1} after 10 cycles at 0.1 A g^{-1}, which is higher than those of the Si (648 mAh g^{-1}) and Si@C (956 mAh g^{-1}). When the current rate increased to 1 A g^{-1}, the Si/CNT@C exhibited a high capacity of 827 mAh g^{-1}, which is obviously much higher than those of the Si (15 mAh g^{-1}) and Si@C (378 mAh g^{-1}). The great improved rate performance of the Si/CNT@C can be attributed to the high conductivity of the CNT matrix and the fast Li^+ ion transmission in the 3D porous structure. When the current density is recovered from 1 to 0.1 A g^{-1}, the capacity of the Si/CNT@C electrode recovers to 852 mAh g^{-1}, which is much higher than the respective capacities of Si (172 mAh g^{-1}) and Si/C (520 mAh g^{-1}), indicating the good reversibility of the Si/CNT@C electrode.

The remarkable discharge capacitance of Si/CNT/C can be ascribed to the synergetic effects of the CNTs and RF resin-derived carbon coating. Firstly, Si NPs were uniformly dispersed in the 3D interconnected CNT matrix and were attached to the CNT sidewall by the amorphous carbon coating shell, forming a 3D nanoporous structured Si/CNT@C composite. The as-developed 3D nanoporous structure facilitates the inhibition of agglomeration of Si NPs, accelerates Li^+ ion transportation, and buffers the volume expansion effect of Si NPs during the delithiation/lithiation process. Secondly, isolated Si NPs were stringed by the CNT matrix, providing a fast electron transport route. Thirdly, the uniform carbon coating layer on the surface of Si NPs and CNTs can restrain the volume expansion effect of Si NPs and thus facilitate the formation of stable SEI film. Based on the above analysis, the Si/CNT@C electrode deserves the greatly enhanced lithium storage capacity and rate capability.

EIS Nquist plots were carried out to eluate the conductivity of the samples. As shown in Figure 4d, all the Nyquist curves reveal a semicircle in the mid-frequency region and a straight line in the low-frequency region, which can be simulated by the inserted equivalent circuit. The R_s, R_{ct}, CPE, and W represent the ohmic resistance of electrolyte and electrode, charge transfer resistance, the constant phase element related to electric double-layer capacitance, and the Warburg impedance, respectively [1,56,62]. As revealed by the fitting results shown in Table S1, the Si/CNT@C electrode shows the smallest R_s (1.6 Ω) and R_{ct} (38.5 Ω), which are much smaller than those of the Si (R_s 2.0 Ω and R_{ct} 92.5 Ω) and Si@C (R_s 1.7 Ω and R_{ct} 62.4 Ω), indicating the significantly enhanced Li^+ ion and electron transportation of the Si/CNT@C electrode. Such significant improvement arises from the synergetic effects of the CNTs and RF resin-derived carbon coating, which enhance the electron transportation between Si NPs and CNTs. The 3D nanoporous structure derived from the CNT matrix also facilitates fast Li^+ ion transportation, which contributes to a rapid de-alloying reaction between Li and Si [75].

Figure 4e shows the cycling stability of the bare Si, Si@C, and Si/CNT@C electrodes at a current rate of 0.1 A g^{-1}. The Si/CNT@C electrode can retain a high specific capacity of 1106 mAh g^{-1} after 200 cycles and its Coulomb efficiency rapidly increased above 99% after the third cycle. In contrast, the Si@C electrode can only retain a relatively low specific capacity of 485 mAh g^{-1} after 200 cycles. As for the bare Si electrode, the specific capacity dramatically decays to almost zero after 200 cycles. Figure S6 shows that the Si/CNT@C electrode can retain a high specific capacity of 770 mAh g^{-1} after cycling at 0.5 A g^{-1} for 200 cycles, further proving its application prospects. As exhibited by Table S2, the Si/CNT@C electrode shows competitively high specific capacity, long cycle stability, and rate capability compared with the recently reported Si-based anode materials, such as SMPS−1 (501 mAh g^{-1} at 1 A g^{-1} after 500 cycles) [70], GSCC (837.3 mAh g^{-1} at 0.2 A g^{-1} after 100 cycles) [66], Si/CNTs/C (702 mAh g^{-1} at 0.2 A g^{-1} after 300 cycles) [71], C/Si/CNT (696.8 mAh g^{-1} at 0.1A g^{-1} after 50 cycles) [72], Si@C@v@CNTs (912.8 mAh g^{-1} at 0.1A g^{-1} after 100 cycles) [73], and Si/CNTs@PMMA−C (1024.8 mAh g^{-1} at 0.2 A g^{-1} after 200 cycles) [78]. The significantly enhanced cycle performance can be attributed to the unique structure advantages of the Si/CNT@C electrode, which can effectively buffer the expansion effect of Si NPs during the delithiation/lithiation process.

4. Conclusions

In this study, a 3D network structured Si/CNT@C composite anode material was synthesized via simple in situ polymerization and the following carbonization strategy. In the as-prepared Si/CNT@C composite, Si NPs were anchored on the surface of CNT, with uniform carbon shells coated on both surfaces of Si NPs and CNT. This unique 3D nanoporous structure, with interconnected CNTs as a supporting matrix, alleviated the agglomeration/volume fluctuation of Si NPs and thereby facilitated fast ion/electron transportation during charge/discharge cycles. As a result, the Si/CNT@C sample retained a high specific capacity of 1106 mAh g^{-1} and 770 mAh g^{-1} after 200 charge/discharge cycles at 0.1 A g^{-1} and 0.5 A g^{-1}, respectively. When the current density increased to 1 A g^{-1}, the Si/CNT@C electrode exhibited a relatively high capacity of 827 mAh g^{-1}. Compared with the bare Si NPs and Si@C samples, the Si/CNT@C exhibited significantly improved cycle stability and rate capability. Considering the easy synthetic route and high Si mass content, the Si/CNT@C composite anode material reported here paves a new way for the industrial application of Si-based anode materials in high-energy LIBs.

Supplementary Materials: The following supporting information can be downloaded at: https://www.mdpi.com/article/10.3390/batteries9020118/s1. Figure S1: Photos of the as-prepared Si/C@RF and Si/CNT@C powder samples. Figure S2: (a,b) SEM images of Si NPs, (c,d) SEM images, and (e,f) TEM images of Si@C composite. Figure S3: Thermogravimetric curves of Si, Si@C and Si/CNT@C samples. Figure S4: (a) CV curves of Si, (b) CV curves of Si@C, and (c) comparison of the third cycle CV curves of the Si, Si@C, and Si/CNT@C. Figure S5: GCD curves of Si (a) and Si@C (b). Figure S6: Cycle performances of the Si/CNT/C electrode at 0.5 A g^{-1}. Table S1: Fitting results of the EIS curves. Table S2: Comparison among the recently reported Si-based anode materials [79,80].

Author Contributions: Conceptualization, H.F. and X.F.; methodology, H.F. and X.F.; software, X.F. and Q.L.; validation, H.F., X.F. and Q.L.; formal analysis, X.F. and Q.L.; investigation, X.F. and Q.L.; resources, X.F. and Q.L.; data curation, X.F. and Q.L.; writing—original draft preparation, H.F. and X.F.; writing—review and editing, L.H., J.Y., and L.W.; visualization, H.F., X.F. and Q.L.; supervision, L.Z., and G.W.; project administration, H.F., L.Z. and G.W.; funding acquisition, H.F., L.Z. and G.W. All authors have read and agreed to the published version of the manuscript.

Funding: This research was funded by Key Scientific Research Project in Colleges and Universities of Henan Province of China (grant number 20B530006) sponsored by Henan Provincial Department of Education, China, and the Science and Technology Project of Henan Province (grant number 222102240122) sponsored by Henan Provincial Department of Science and Technology, China.

Institutional Review Board Statement: Not applicable.

Informed Consent Statement: Not applicable.

Data Availability Statement: Not applicable.

Conflicts of Interest: The authors declare no conflicts of interest.

References

1. Ma, T.; Xu, H.; Yu, X.; Li, H.; Zhang, W.; Cheng, X.; Zhu, W.; Qui, X. Lithiation Behavior of Coaxial Hollow Nanocables of Carbon-Silicon Composite. *ACS Nano* **2019**, *13*, 2274–2280.
2. Salah, M.; Murphy, P.; Hall, C.; Francis, C.; Kerr, R.; Fabretto, M. Pure Silicon Thin-Film Anodes for Lithium-Ion Batteries: A Review. *J. Power Sources* **2019**, *414*, 48–67.
3. Wang, F.; Lin, S.; Lu, X.; Hong, R.; Liu, H. Poly-Dopamine Carbon-Coated Stable Silicon/Graphene/CNT Composite as Anode for Lithium Ion Batteries. *Electrochim. Acta* **2022**, *404*, 139708.
4. Wang, H.W.; Fu, J.Z.; Wang, C.; Wang, J.Y.; Yang, A.K.; Li, C.C.; Sun, Q.F.; Cui, Y.; Li, H.Q. A Binder-Free High Silicon Content Flexible Anode for Li-Ion Batteries. *Energy Environ. Sci.* **2020**, *13*, 848–858.
5. Ko, M.; Chae, S.; Ma, J.; Kim, N.; Lee, H.-W.; Cui, Y.; Cho, J. Scalable Synthesis of Silicon-Nanolayer-Embedded Graphite for High-Energy Lithium-Ion Batteries. *Nat. Energy* **2016**, *1*, 16113.
6. Lv, X.; Wei, W.; Huang, B.; Dai, Y. Achieving High Energy Density for Lithium-Ion Battery Anodes by Si/C Nanostructure Design. *J. Mater. Chem. A* **2019**, *7*, 2165–2171.

7. Zhang, L.; Wang, C.; Dou, Y.; Cheng, N.; Cui, D.; Du, Y.; Liu, P.; Al-Mamun, M.; Zhang, S.; Zhao, H. A Yolk-Shell Structured Silicon Anode with Superior Conductivity and High Tap Density for Full Lithium-Ion Batteries. *Angew. Chem. Int. Ed.* **2019**, *58*, 8824–8828.
8. Zhang, C.; Wang, F.; Han, J.; Bai, S.; Tan, J.; Liu, J.; Li, F. Challenges and Recent Progress on Silicon-Based Anode Materials for Next-Generation Lithium-Ion Batteries. *Small Struct.* **2021**, *2*, 2100009.
9. Wang, Z.; Jing, L.; Zheng, X.; Xu, Z.; Yuan, Y.; Liu, X.; Fu, A.; Guo, Y.-G.; Li, H. Microspheres of Si@Carbon-CNTs Composites with a Stable 3D Interpenetrating Structure Applied in High-Performance Lithium-Ion Battery. *J. Colloid Interface Sci.* **2022**, *629*, 511–521.
10. Wei, R.; Liu, X.Q.; Tian, Y.; Huang, F.F.; Xu, S.Q.; Zhang, J.J. Sn-Based Glass-Graphite-Composite as a High Capacity Anode for Lithium-Ion Batteries. *J. Am. Ceram. Soc.* **2023**, *106*, 330–338.
11. Nurpeissova, A.; Adi, A.; Aishova, A.; Mukanova, A.; Kim, S.S.; Bakenov, Z. Synergistic Effect of 3D Current Collector Structure and Ni Inactive Matrix on the Electrochemical Performances of Sn-Based Anodes for Lithium-Ion Batteries. *Mater. Today Energy* **2020**, *16*, 100397.
12. Chen, Y.; Zou, Y.M.; Shen, X.P.; Qiu, J.X.; Lian, J.B.; Pu, J.R.; Li, S.; Du, F.H.; Li, S.Q.; Ji, Z.Y.; et al. Ge Nanoparticles Uniformly Immobilized on 3D Interconnected Porous Graphene Frameworks as Anodes for High-Performance Lithium-Ion Batteries. *J. Energy Chem.* **2022**, *69*, 161–173.
13. Wang, Y.R.; Zhuang, Q.F.; Li, Y.; Hu, Y.L.; Liu, Y.Y.; Zhang, Q.B.; Shi, L.; He, C.X.; Zheng, X.; Yu, S.H. Bio-Inspired Synthesis of Transition-Metal Oxide Hybrid Ultrathin Nanosheets for Enhancing the Cycling Stability in Lithium-Ion Batteries. *Nano Res.* **2022**, *15*, 5064–5071.
14. Hou, T.; Liu, B.; Sun, X.; Fan, A.; Xu, Z.; Cai, S.; Zheng, C.; Yu, G.; Tricoli, A. Covalent Coupling-Stabilized Transition-Metal Sulfide/Carbon Nanotube Composites for Lithium/Sodium-Ion Batteries. *ACS Nano* **2021**, *15*, 6735–6746.
15. Shen, M.; Ma, H. Metal-Organic Frameworks (MOFs) and Their Derivative as Electrode Materials for Lithium-Ion Batteries. *Coord. Chem. Rev.* **2022**, *470*, 214715.
16. Li, P.; Hwang, J.-Y.; Sun, Y.-K. Nano/Microstructured Silicon-Graphite Composite Anode for High-Energy-Density Li-Ion Battery. *ACS Nano* **2019**, *13*, 2624–2633.
17. Fang, S.; Shen, L.; Li, S.; Kim, G.-T.; Bresser, D.; Zhang, H.; Zhang, X.; Maier, J.; Passerini, S. Alloying Reaction Confinement Enables High-Capacity and Stable Anodes for Lithium-Ion Batteries. *ACS Nano* **2019**, *13*, 9511–9519.
18. Zhang, Y.; Li, B.; Tang, B.; Yao, Z.; Zhang, X.; Liu, Z.; Gong, R.; Zhao, P. Mechanical Constraining Double-Shell Protected Si-Based Anode Material for Lithium-Ion Batteries with Long-Term Cycling Stability. *J. Alloys Compd.* **2020**, *846*, 156437.
19. Zhao, Z.; Cai, M.; Zhao, H.; Ma, Q.; Xie, H.; Xing, P.; Zhuang, Y.X.; Yin, H. Harvesting Si Nanostructures and C-Si Composites by Paired Electrolysis in Molten Salt: Implications for Lithium Storage. *ACS Appl. Nano Mater.* **2022**, *5*, 3781–3789.
20. Chae, S.; Choi, S.-H.; Kim, N.; Sung, J.; Cho, J. Integration of Graphite and Silicon Anodes for the Commercialization of High-Energy Lithium-Ion Batteries. *Angew. Chem. Int. Ed.* **2020**, *59*, 110–135.
21. Zhao, J.; Wei, W.; Xu, N.; Wang, X.; Chang, L.; Wang, L.; Fang, L.; Le, Z.; Nie, P. Dealloying Synthesis of Silicon Nanotubes for High-Performance Lithium Ion Batteries. *ChemPhysChem* **2022**, *23*, e202100832.
22. Wang, F.; Ma, Y.; Li, P.; Peng, C.; Yin, H.; Li, W.; Wang, D. Electrochemical Conversion of Silica Nanoparticles to Silicon Nanotubes in Molten Salts: Implications for High-Performance Lithium-Ion Battery Anode. *ACS Appl. Nano Mater.* **2021**, *4*, 7028–7036.
23. Yan, Z.; Jiang, J.; Zhang, Y.; Yang, D.; Du, N. Scalable and Low-Cost Synthesis of Porous Silicon Nanoparticles as High-Performance Lithium-Ion Battery Anode. *Mater. Today Nano* **2022**, *18*, 100175.
24. Chen, Y.; Liu, L.F.; Xiong, J.; Yang, T.Z.; Qin, Y.; Yan, C.L. Porous Si Nanowires from Cheap Metallurgical Silicon Stabilized by a Surface Oxide Layer for Lithium Ion Batteries. *Adv. Funct. Mater.* **2015**, *25*, 6701–6709.
25. Pathak, A.D.; Chanda, U.K.; Samanta, K.; Mandal, A.; Sahu, K.K.; Pati, S. Selective Leaching of Al from Hypereutectic Al-Si Alloy to Produce Nano-Porous Silicon (NPs) Anodes for Lithium Ion Batteries. *Electrochim. Acta* **2019**, *317*, 654–662.
26. Huang, X.; Ding, Y.C.; Li, K.L.; Guo, X.Y.; Zhu, Y.; Zhang, Y.X.; Bao, Z.H. Spontaneous Formation of the Conformal Carbon Nanolayer Coated Si Nanostructures as the Stable Anode for Lithium-Ion Batteries from Silica Nanomaterials. *J. Power Sources* **2021**, *496*, 229833.
27. Hailu, A.G.; Ramar, A.; Wang, F.M.; Wu, N.L.; Yeh, N.H.; Hsu, C.C.; Chang, Y.J.; Tiong, P.W.L.; Yuwono, R.A.; Khotimah, C.; et al. Investigations of Intramolecular Hydrogen Bonding Effect of a Polymer Brush Modified Silicon in Lithium-Ion Batteries. *Adv. Mater. Interfaces* **2022**, *9*, 2102007.
28. Yu, C.H.; Chen, X.; Xiao, Z.X.; Lei, C.; Zhang, C.X.; Lin, X.Q.; Shen, B.Y.; Zhang, R.F.; Wei, F. Silicon Carbide as a Protective Layer to Stabilize Si-Based Anodes by Inhibiting Chemical Reactions. *Nano Lett.* **2019**, *19*, 5124–5132.
29. Gao, X.; Lu, W.Q.; Xu, J. Unlocking Multiphysics Design Guidelines on Si/C Composite Nanostructures for High-Energy-Density and Robust Lithium-Ion Battery Anode. *Nano Energy* **2021**, *81*, 105591.
30. Bitew, Z.; Tesemma, M.; Beyene, Y.; Amare, M. Nano-Structured Silicon and Silicon Based Composites as Anode Materials for Lithium Ion Batteries: Recent Progress and Perspectives. *Sustain. Energy Fuels* **2022**, *6*, 1014–1050.
31. She, Z.M.; Uceda, M.; Pope, M.A. Encapsulating a Responsive Hydrogel Core for Void Space Modulation in High-Stability Graphene-Wrapped Silicon Anodes. *ACS Appl. Mater. Interfaces* **2022**, *14*, 10363–10372.
32. Yang, Z.X.; Du, Y.; Yang, Y.J.; Jin, H.C.; Shi, H.B.; Bai, L.Y.; Ouyang, Y.G.; Ding, F.; Hou, G.L.; Yuan, F.L. Large-Scale Production of Highly Stable Silicon Monoxide Nanowires by Radio-Frequency Thermal Plasma as Anodes for High-Performance Li-Ion Batteries. *J. Power Sources* **2021**, *497*, 229906.

33. Chen, S.Y.; Xu, Y.N.; Du, H.B. One-Step Synthesis of Uniformly Distributed SiO_x-C Composites as Stable Anodes for Lithium-Ion Batteries. *Dalton Trans.* **2022**, *51*, 11909–11915.
34. Gu, H.T.; Wang, Y.; Zeng, Y.; Yu, M.; Liu, T.; Chen, J.; Wang, K.; Xie, J.Y.; Li, L.S. Boosting Cyclability and Rate Capability of SiO_x via Dopamine Polymerization-Assisted Hybrid Graphene Coating for Advanced Lithium-Ion Batteries. *ACS Appl. Mater. Interfaces* **2022**, *14*, 17388–17395.
35. Di, S.H.; Zhang, D.X.; Weng, Z.; Chen, L.; Zhang, Y.; Zhang, N.; Ma, R.Z.; Chen, G.; Liu, X.H. Crosslinked Polymer Binder via Phthalic Acid for Stabilizing SiO_x Anodes. *Macromol. Chem. Phys.* **2022**, *223*, 2200068.
36. Zhao, J.K.; Wei, D.A.; Wang, J.J.; Yang, K.M.; Wang, Z.L.; Chen, Z.J.; Zhang, S.G.; Zhang, C.; Yang, X.J. Inorganic Crosslinked Supramolecular Binder with Fast Self-Healing for High Performance Silicon Based Anodes in Lithium-Ion Batteries. *J. Colloid Interface Sci.* **2022**, *625*, 373–382.
37. Kim, J.; Park, Y.K.; Kim, H.; Jung, I.H. Ambidextrous Polymeric Binder for Silicon Anodes in Lithium-Ion Batteries. *Chem. Mater.* **2022**, *34*, 5791–5798.
38. Rajeev, K.K.; Jang, W.; Kim, S.; Kim, T.H. Chitosan-Grafted-Gallic Acid as a Nature-Inspired Multifunctional Binder for High-Performance Silicon Anodes in Lithium-Ion Batteries. *ACS Appl. Energy Mater.* **2022**, *5*, 3166–3178.
39. Deng, L.; Zheng, Y.; Zheng, X.M.; Or, T.; Ma, Q.Y.; Qian, L.T.; Deng, Y.P.; Yu, A.P.; Li, J.T.; Chen, Z.W. Design Criteria for Silicon-Based Anode Binders in Half and Full Cells. *Adv. Energy Mater.* **2022**, *12*, 2200850.
40. Li, H.; Li, H.; Lai, Y.; Yang, Z.; Yang, Q.; Liu, Y.; Zheng, Z.; Liu, Y.; Sun, Y.; Zhong, B.; et al. Revisiting the Preparation Progress of Nano-Structured Si Anodes toward Industrial Application from the Perspective of Cost and Scalability. *Adv. Energy Mater.* **2022**, *12*, 2102181.
41. Wu, Z.; Kong, D. Comparative Life Cycle Assessment of Lithium-Ion Batteries with Lithium Metal, Silicon Nanowire, and Graphite Anodes. *Clean Technol. Environ. Policy* **2018**, *20*, 1233–1244.
42. Maxwell, T.L.; Balk, T.J. The Fabrication and Characterization of Bimodal Nanoporous Si with Retained Mg through Dealloying. *Adv. Eng. Mater.* **2018**, *20*, 1700519.
43. Wang, X.; Wen, K.; Chen, T.; Chen, S.; Zhang, S. Supercritical Fluid-Assisted Preparation of Si/CNTs@FG Composites with Hierarchical Conductive Networks as a High-Performance Anode Material. *Appl. Surf. Sci.* **2020**, *522*, 146507.
44. Yang, Y.; Yuan, W.; Kang, W.; Ye, Y.; Yuan, Y.; Qiu, Z.; Wang, C.; Zhang, X.; Ke, Y.; Tang, Y. Silicon-Nanoparticle-Based Composites for Advanced Lithium-Ion Battery Anodes. *Nanoscale* **2020**, *12*, 7461–7484.
45. Liu, L.; Lyu, J.; Li, T.; Zhao, T. Well-Constructed Silicon-Based Materials as High-Performance Lithium-Ion Battery Anodes. *Nanoscale* **2016**, *8*, 701–722.
46. Li, Y.; Liu, X.; Zhang, J.; Yub, H.; Zhang, J. Carbon-Coated Si/N-Doped Porous Carbon Nanofibre Derived from Metal-Organic Frameworks for Li-Ion Battery Anodes. *J. Alloys Compd.* **2022**, *902*, 163635.
47. Zeng, Y.; Huang, Y.; Liu, N.; Wang, X.; Zhang, Y.; Guo, Y.; Wu, H.-H.; Chen, H.; Tang, X.; Zhang, Q. N-Doped Porous Carbon Nanofibers Sheathed Pumpkin-Like Si/C Composites as Free-Standing Anodes for Lithium-Ion Batteries. *J. Energy Chem.* **2021**, *54*, 727–735.
48. Park, B.H.; Lee, G.-W.; Choi, S.B.; Kim, Y.-H.; Kim, K.B. Triethoxysilane-Derived SiO_x-Assisted Structural Reinforcement of Si/Carbon Nanotube Composite for Lithium-Ion Battery. *Nanoscale* **2020**, *12*, 22140–22149.
49. Yi, Z.; Lin, N.; Zhao, Y.; Wang, W.; Qian, Y.; Zhu, Y.; Qian, Y. A Flexible Micro/Nanostructured Si Microsphere Cross-Linked by Highly-Elastic Carbon Nanotubes toward Enhanced Lithium Ion Battery Anodes. *Energy Storage Mater.* **2019**, *17*, 93–100.
50. Liu, X.; Sun, X.; Shi, X.; Song, D.; Zhang, H.; Li, C.; Wang, K.-Y.; Xiao, C.; Liu, X.; Zhang, L. Low-Temperature and High-Performance Si/Graphite Composite Anodes Enabled by Sulfite Additive. *Chem. Eng. J.* **2021**, *421*, 127782.
51. Zhao, E.; Luo, S.; Gu, Y.; Yang, L.; Hirano, S.-I. Preactivation Strategy for a Wide Temperature Range in Situ Gel Electrolyte-Based $LiNi_{0.5}Co_{0.2}Mn_{0.3}O_2$ Parallel to Si-Graphite Battery. *ACS Appl. Mater. Interfaces* **2021**, *13*, 59843–59854.
52. Liu, P.; Sun, X.; Xu, Y.; Wei, C.; Liang, G. By Self-Assembly of Electrostatic Attraction to Encapsulate Protective Carbon-Coated Nano-Si into Graphene for Lithium-Ion Batteries. *Ionics* **2022**, *28*, 1099–1108.
53. Ren, Y.; Xiang, L.; Yin, X.; Xiao, R.; Zuo, P.; Gao, Y.; Yin, G.; Du, C. Ultrathin Si Nanosheets Dispersed in Graphene Matrix Enable Stable Interface and High Rate Capability of Anode for Lithium-Ion Batteries. *Adv. Funct. Mater.* **2022**, *32*, 2110046.
54. Shao, F.; Li, H.; Yao, L.; Xu, S.; Li, G.; Li, B.; Zou, C.; Yang, Z.; Su, Y.; Hu, N.; et al. Binder-Free, Flexible, and Self-Standing Non-Woven Fabric Anodes Based on Graphene/Si Hybrid Fibers for High-Performance Li-Ion Batteries. *ACS Appl. Mater. Interfaces* **2021**, *13*, 27270–27277.
55. Zhang, H.; Zhang, X.; Jin, H.; Zong, P.; Bai, Y.; Lian, K.; Xu, H.; Ma, F. A Robust Hierarchical 3D Si/CNTs Composite with Void and Carbon Shell as Li-Ion Battery Anodes. *Chem. Eng. J.* **2019**, *360*, 974–981.
56. Yang, Y.; Li, J.; Chen, D.; Fu, T.; Sun, D.; Zhao, J. Binder-Free Carbon-Coated Silicon–Reduced Graphene Oxide Nanocomposite Electrode Prepared by Electrophoretic Deposition as a High-Performance Anode for Lithium-Ion Batteries. *ChemElectroChem* **2016**, *3*, 757–763.
57. An, W.; Xiang, B.; Fu, J.; Mei, S.; Guo, S.; Huo, K.; Zhang, X.; Gao, B.; Chu, P.K. Three-Dimensional Carbon-Coating Silicon Nanoparticles Welded on Carbon Nanotubes Composites for High-Stability Lithium-Ion Battery Anodes. *Appl. Surf. Sci.* **2019**, *479*, 896–902.
58. Luo, W.; Wang, Y.; Chou, S.; Xu, Y.; Li, W.; Kong, B.; Dou, S.X.; Liu, H.K.; Yang, J. Critical Thickness of Phenolic Resin-Based Carbon Interfacial Layer for Improving Long Cycling Stability of Silicon Nanoparticle Anodes. *Nano Energy* **2016**, *27*, 255–264.

59. Fang, H.; Zou, W.; Yan, J.; Xing, Y.; Zhang, S. Facile Fabrication of Fe_2O_3 Nanoparticles Anchored on Carbon Nanotubes as High-Performance Anode for Lithium-Ion Batteries. *ChemElectroChem* **2018**, *5*, 2458–2463.
60. Guan, B.; Wang, X.; Xiao, Y.; Liu, Y.; Huo, Q. A Versatile Cooperative Template-Directed Coating Method to Construct Uniform Microporous Carbon Shells for Multifunctional Core-Shell Nanocomposites. *Nanoscale* **2013**, *5*, 2469–2475.
61. Ma, X.Y.; Yin, Z.L.; Tong, H.; Yu, S.; Li, Y.; Ding, Z.Y. 3D Graphene-Like Nanosheets/Silicon Wrapped by Catalytic Graphite as a Superior Lithium Storage Anode. *J. Electroanal. Chem.* **2020**, *873*, 114350.
62. Wang, M.-S.; Wang, Z.-Q.; Jia, R.; Yang, Y.; Zhu, F.-Y.; Yang, Z.-L.; Huang, Y.; Li, X.; Xu, W. Facile Electrostatic Self-Assembly of Silicon/Reduced Graphene Oxide Porous Composite by Silica Assist as High Performance Anode for Li-Ion Battery. *Appl. Surf. Sci.* **2018**, *456*, 379–389.
63. Wang, B.; Li, X.L.; Zhang, X.F.; Luo, B.; Jin, M.H.; Liang, M.H.; Dayeh, S.A.; Picraux, S.T.; Zhi, L.J.; Adaptable Silicon-Carbon Nanocables Sandwiched between Reduced Graphene Oxide Sheets as Lithium Ion Battery Anodes. *ACS Nano* **2013**, *7*, 1437–1445.
64. Guo, C.Z.; Liao, W.L.; Li, Z.B.; Sun, L.T.; Chen, C.G. Easy Conversion of Protein-Rich Enoki Mushroom Biomass to a Nitrogen-Doped Carbon Nanomaterial as a Promising Metal-Free Catalyst for Oxygen Reduction Reaction. *Nanoscale* **2015**, *7*, 15990–15998.
65. Ma, C.; Wang, Z.; Zhao, Y.; Li, Y.; Shi, J. A Novel Raspberry-Like Yolk-Shell Structured Si/C Micro/Nano-Spheres as High-Performance Anode Materials for Lithium-Ion Batteries. *J. Alloys Compd.* **2020**, *844*, 156201.
66. Huang, Y.; Li, W.; Peng, J.; Wu, Z.; Li, X.; Wang, X. Structure Design and Performance of the Graphite/Silicon/Carbon Nanotubes/Carbon (GSCC) Composite as the Anode of a Li-Ion Battery. *Energy Fuels* **2021**, *35*, 13491–13498.
67. Wang, S.; Liao, J.; Wu, M.; Xu, Z.; Gong, F.; Chen, C.; Wang, Y.; Yan, X. High Rate and Long Cycle Life of a CNT/RGO/Si Nanoparticle Composite Anode for Lithium-Ion Batteries. *Part. Part. Syst. Charact.* **2017**, *34*, 1700141.
68. Ramachandran, A.; Sarojiniamma, S.; Varatharajan, P.; Appusamy, I.S.; Yesodha, S.K. Nano Graphene Shell for Silicon Nanoparticles: A Novel Strategy for a High Stability Rechargeable Battery Anode. *ChemistrySelect* **2018**, *3*, 11190–11199.
69. Zhu, X.; Choi, S.H.; Tao, R.; Jia, X.; Lu, Y. Building High-Rate Silicon Anodes Based on Hierarchical Si@C@CNT Nanocomposite. *J. Alloys Compd.* **2019**, *791*, 1105–1113.
70. Xu, R.; Wei, R.; Hu, X.; Li, Y.; Wang, L.; Zhang, K.; Wang, Y.; Zhang, H.; Liang, F.; Yao, Y. A Strategy and Detailed Explanations to the Composites of Si/MWCNTs for Lithium Storage. *Carbon* **2021**, *171*, 265–275.
71. Fu, Z.; Bian, F.; Ma, J.; Zhang, W.; Gan, Y.; Xia, Y.; Zhang, J.; He, X.; Huang, H. In Situ Synthesis of a Si/CNTs/C Composite by Directly Reacting Magnesium Silicide with Lithium Carbonate for Enhanced Lithium Storage Capability. *Energy Fuels* **2021**, *35*, 20386–20393.
72. Kong, X.; Luo, S.; Rong, L.; Xie, X.; Zhou, S.; Chen, Z.; Pan, A. Enveloping a Si/N-Doped Carbon Composite in a CNT-Reinforced Fibrous Network as Flexible Anodes for High Performance Lithium-Ion Batteries. *Inorg. Chem. Front.* **2021**, *8*, 4386–4394.
73. Han, N.; Li, J.; Wang, X.; Zhang, C.; Liu, G.; Li, X.; Qu, J.; Peng, Z.; Zhu, X.; Zhang, L. Flexible Carbon Nanotubes Confined Yolk-Shelled Silicon-Based Anode with Superior Conductivity for Lithium Storage. *Nanomaterials* **2021**, *11*, 699.
74. Liu, W.; Hu, Y.; Qiao, Y.; Jiang, J.; Huang, M.; Qu, M.; Peng, G.; Xie, Z. 1-Aminopyrene-Modified Functionalized Carbon Nanotubes Wrapped with Silicon as a High-Performance Lithium-Ion Battery Anode. *Solid State Ion.* **2021**, *369*, 115724.
75. Park, G.D.; Choi, J.H.; Jung, D.S.; Park, J.-S.; Kang, Y.C. Three-Dimensional Porous Pitch-Derived Carbon Coated Si Nanoparticles-CNT Composite Microsphere with Superior Electrochemical Performance for Lithium Ion Batteries. *J. Alloys Compd.* **2020**, *821*, 153224.
76. Liang, J.; Li, X.; Hou, Z.; Zhang, W.; Zhu, Y.; Qian, Y. A Deep Reduction and Partial Oxidation Strategy for Fabrication of Mesoporous Si Anode for Lithium Ion Batteries. *ACS Nano* **2016**, *10*, 2295–2304.
77. Luo, Z.; Xiao, Q.; Lei, G.; Li, Z.; Tang, C. Si Nanoparticles/Graphene Composite Membrane for High Performance Silicon Anode in Lithium Ion Batteries. *Carbon* **2016**, *98*, 373–380.
78. Shi, J.; Jiang, X.; Ban, B.; Li, J.; Chen, J. Carbon Nanotubes-Enhanced Lithium Storage Capacity of Recovered Silicon/Carbon Anodes Produced from Solar-Grade Silicon Kerf Scrap. *Electrochim. Acta* **2021**, *381*, 138269.
79. Liang, A.-H.; Xu, T.-H.; Liou, S.; Li, Y.-Y. Silicon Single Walled Carbon Nanotube-Embedded Pitch-Based Carbon Spheres Prepared by a Spray Process with Modified Antisolvent Precipitation for Lithium Ion Batteries. *Energy Fuels* **2021**, *35*, 9705–9713.
80. Saha, S.; Jana, M.; Khanra, P.; Samanta, P.; Koo, H.; Chandra Murmu, N.; Kuila, T. Band gap modified boron doped NiO/Fe3O4 nanostructure as the positive electrode for high energy asymmetric supercapacitors. *RSC Adv.* **2016**, *6*, 1380–1387.